Review Article

Nano Research
2021, 14(6): 1802–1813

ISSN 1998-0124 CN 11-5974/O4
https://doi.org/10.1007/s12274-020-2860-3

Ferromagnetic and ferroelectric two-dimensional materials for memory application

Zhen Liu[1,2,3], Longjiang Deng[1,2,3], and Bo Peng[1,2,3] (✉)

[1] *National Engineering Research Center of Electromagnetic Radiation Control Materials, School of Electronic Science and Engineering, University of Electronic Science and Technology of China, Chengdu 611731, China*
[2] *Key Laboratory of Multi-spectral Absorbing Materials and Structures of Ministry of Education, University of Electronic Science and Technology of China, Chengdu 611731, China*
[3] *State Key Laboratory of Electronic Thin Films and Integrated Devices, University of Electronic Science and Technology of China, Chengdu 611731, China*

Received: 7 March 2020; **Revised:** 29 April 2020; **Accepted:** 8 May 2020

ABSTRACT

The discoveries of ferromagnetic and ferroelectric two-dimensional (2D) materials have dramatically inspired intense interests due to their potential in the field of spintronic and nonvolatile memories. This review focuses on the latest 2D ferromagnetic and ferroelectric materials that have been most recently studied, including insulating ferromagnetic, metallic ferromagnetic, antiferromagnetic and ferroelectric 2D materials. The fundamental properties that lead to the long-range magnetic orders of 2D materials are discussed. The low Curie temperature (T_c) and instability in 2D systems limits their use in practical applications, and several strategies to address this constraint are proposed, such as gating and composition stoichiometry. A van der Waals (vdW) heterostructure comprising 2D ferromagnetic and ferroelectric materials will open a door to exploring exotic physical phenomena and achieve multifunctional or nonvolatile devices.

KEYWORDS

two-dimensional (2D) materials, ferromagnetic, ferroelectric, heterostructure, nonvolatile memory

1 Introduction

In the 1930s, Landau and Peierls concluded that no two-dimensional (2D) crystalline long-range order can survive at any finite temperature owing to the thermal fluctuation [1–3]. In 1966, Mermin and Wagner predicted "absence of ferromagnetism or antiferromagnetism in one-dimensional (1D) or 2D isotropic Heisenberg models at any non-zero temperature" [4], and further deduced no 2D crystalline long-range order [5], which is currently accepted as "Mermin-Wagner Theorem". However, in 2004, Geim A. and Novoselov K. discovered a flat flake of carbon with a thickness of just one atom—graphene [6], realizing the groundbreaking experiments in the 2D models, which induced a fundamental transformation in 2D materials. The discovery of graphene has inspired scientists to extensively explore the family of 2D van der Waals (vdW) materials more than ever before, and ultimately uncover plenty of unique optical, electrical, mechanical and thermal properties in 2D systems very different from their own properties in bulk materials. Through the wonders of 2D layered materials, 2D materials display metallic [7], semiconducting [8], superconducting [9], insulating and ferroelectric [10–12] properties. However, the Mermin-Wagner theorem was suppressing the achievement of 2D ferromagnetism until 2017, when long-range magnetic orders were experimentally discovered in CrI_3 and $Cr_2Ge_2Te_6$ down to the monolayer limit [13, 14], which represent another paradigm shift in the field of 2D materials.

Ferromagnetism, refers to a permanent magnetic moment without applying any external magnetic field when the temperature is below a critical value-Curie temperature (T_c). Through the ages, the three-dimensional (3D) ferromagnetic with high T_c can be easily achieved. However, the absence of 2D ferromagnetic is a long-standing issue. According to the Mermin-Wanger theorem, the finite-range exchange interaction cannot preserve the long-range magnetic orders which can be destroyed by the thermal fluctuation at nonzero temperature [4]. Cutting through the limitation of Mermin-Wanger theorem requires strong enough magnetic anisotropy overcoming the thermal fluctuation like the way the 2D Ising model are. Thus, introducing magnetocrystalline anisotropy, shape anisotropy, exchange anisotropy and magnetoelastic anisotropy, will make the way to long-range magnetic order at finite temperature and 2D ferromagnetism possible. It should be made clear, in parentheses, that the layered vdW magnetic bulk crystals have been discovered in 1960s [15, 16]. But until now, through the wonders of growth and exfoliation technology, mono/few-layer ferromagnetism is realized by mechanically exfoliating from the chemical vapor transport (CVT) grown bulks.

In the meantime, a few atomically thin magnets have been prepared on 2D non-magnetic materials via extrinsic methods, such as defect engineering [17–20], doping control [21–24] and surface functionalization [20, 25, 26], etc. Nevertheless, limited by the destructive effect in material and weak magnetism, there remain debates on the origin of the magnetism; and it is

Address correspondence to bo_peng@uestc.edu.cn

difficult to put them into practice. In 2016, few-layered antiferromagnetic $NiPS_3$ [27], $FePS_3$ [28, 29] and $CrSiTe_3$ [30] were exfoliated from magnetic 2D bulk materials. The significant breakthrough took place in 2017, the unambiguous experiments of ferromagnetism in atomically thin monolayer CrI_3 [13] and trilayer $Cr_2Ge_2Te_6$ [14], respectively. Ever after, experimental lists of ferromagnetic examples of Fe_3GeTe_2 [31], VSe_2 [32] and $MnSe_2$ [33] have been reported in succession. Except for the experimental efforts, a set of 2D ferromagnetic materials were predicted via density functional theory (DFT) calculation, such as transition metal dichalcogenides [32, 34, 35], transition metal trichalcogenides [14, 30, 36, 37], trihalides [13, 38–41], MXenes [42–46] and other materials [31, 47–54]. The summarized details of the partial theoretical and experimental 2D ferromagnetic materials have been illustrated in Table 1.

As another vital type of 2D vdW materials, ferroelectric materials with a non-centrosymmetric structure shows huge potential in electric devices and nanoscale electromechanical systems. For the record, ferroelectric by definition is a type of materials with spontaneous polarization in the absence of external electric field below the T_c. The polarization could be switched and controlled through an external electric field, which unlocks plenty of application opportunities for field-effect transistors (FET) [55], nonvolatile random access memory (RAM) [56, 57], sensors and photonic devices [58, 59], etc. As early as 1920s, the ferroelectric has been discovered [60], however, to date, the stable polarization of traditional ferroelectric materials are only maintained above a critical thickness of approximately ten of nanometers, otherwise the synergetic effects of depolarization and electric dipoles will occur [61–64].

Higher density, lower-consumption and ultra-sensitive electrics are urgently needed for modern technology, and ferroelectric devices happen to suit this need with reduced dimensions. So far, lots of attentions have been devoted to perovskite oxide thin films (such as $PbTiO_3$ [61], $BaTiO_3$ [65] and $BiFeO_3$ [66]) and simple binary oxides (HfO_2 [67] and ZrO_2 [68]), the ferroelectric could be retained down to several unit cells. Nevertheless, the elaborate design of lattice-matched growth substrates or complex preparation processes are inevitable to achieve high-quality ferroelectric thin films at nanoscale, which restricts their practical applications in modern nanoscale electric devices. 2D vdW layered materials provide opportunities to overcome this constraint to some extent owing to the unique strong intralayer coupling and weak interlayer interaction, which can be easily integrated into substrates, making them become promising candidates in realizing low-dimensional ferroelectric devices. To date, abundant 2D ferroelectric materials have been theoretically predicted, including monolayer distorted 1T-phase transition metal chalcogenides with a formula of MX_2 (M = Mo, W; X = S, Se, Te) [69–71], low-buckled honeycomb AB binary monolayer (A and B originate from group IV or III–V) [72, 73], III_2–V_3 compounds (such as In_2Se_3) [11], graphitic binary compound bilayer (such as BN, AlN, ZnO, GaSe) [73] and transition metal thiophosphate (such as $AgBiP_2Se_6$, $CuInP_2S_6$ and $CuInP_2Se_6$) [74–76] and other materials [73, 77–82]. In contrary, experimental reports on 2D ferroelectric materials remain uncommon. At present, only the following 2D ferroelectric materials of 1T-$MoTe_2$ [12], WTe_2 [83], α-In_2Se_3 [11], β'-In_2Se_3 [84], SnTe [85], $CuInP_2S_6$ [86], BA_2PbCl_4 [87], have been experimentally reported. In order to make readers more intuitive, parts of the theoretical and experimental results have been summarized in Table 2.

The strong covalent-bonded intralayer coupling and weak vdW interlayer interaction of 2D material hold great potential in constructing heterostructure devices and achieving multi-functional applications. Upon external perturbations (light, strain, gating and proximity, etc.), 2D vdW ferromagnetism and ferroelectrics will give rise to more exotic quantum phenomena and provide more opportunities in device applications. Particularly, 2D ferromagnetic and ferroelectric heterostructures attract intense interest and open numerous opportunities for spintronic, sensor and nonvolatile memory devices. In this review, we will give a general overview about the rapid progress in 2D vdW ferromagnetic and ferroelectric. This paper is

Table 1 2D ferromagnetic materials

Material	T_c (K)	Research status	Ref.	Material	T_c (K)	Research status	Ref.
VS_2	90	Theoretical	[34]	Mn_2NF_2	1,877	Theoretical	[42]
VSe_2	300	Experimental	[32]	Mn_2NO_2	1,379	Theoretical	[42]
MnS_2	225	Theoretical	[35]	Mn_2CO_2	110	Theoretical	[43]
$MnSe_2$	250	Theoretical	[35]	Mn_2CCl_2	380	Theoretical	[43]
$CrGeTe_3$	57/106	Theoretical	[36]	Mn_2CH_2	120	Theoretical	[43]
$CrSiTe_3$	36/80	Theoretical	[30]	Cr_3C_2	886	Theoretical	[44]
$CrSnTe_3$	170	Theoretical	[37]	Cr_2NO_2	566	Theoretical	[45]
$Cr_2Ge_2Te_6$	30	Experimental	[14]	Fe_2C	861	Theoretical	[46]
CrI_3	45	Experimental	[13]	Fe_2Si	780	Theoretical	[47]
$CrBr_3$	73	Theoretical	[38]	FeC_2	245	Theoretical	[48]
$CrCl_3$	49	Theoretical	[38]	Fe_3GeTe_2	206	Experimental	[31]
CrF_3	41	Theoretical	[38]	MnO_2	140	Theoretical	[49]
VI_3	98	Theoretical	[39]	Mn_3O_4	45	Theoretical	[50]
VCl_3	80	Theoretical	[39]	Cu_2MoS_4	350	Theoretical	[51]
MnI_3	720	Theoretical	[40]	K_2CuF_4	8	Theoretical	[52]
$MnBr_3$	700	Theoretical	[40]	CrN	675	Theoretical	[53]
$MnCl_3$	680	Theoretical	[40]	Co_2S_2	404	Theoretical	[54]
MnF_3	450	Theoretical	[40]				
RuI_3	360	Theoretical	[41]				

Table 2 2D ferroelectric materials

Material	T_c (K)	polarization	Research status	Ref.	Material	T_c (K)	polarization	Research status	Ref.
d1T-MoS_2	> RT	Out-of-plane	Theoretical	[69]	GaN	—	Out-of-plane	Theoretical	[73]
t-MoS_2	—	Out-of-plane	Theoretical	[70]	GaSe	—	Out-of-plane	Theoretical	[73]
t-$MoSe_2$	—	Out-of-plane	Theoretical	[70]	SiC	—	Out-of-plane	Theoretical	[73]
t-$MoTe_2$	—	Out-of-plane	Theoretical	[70]	BN	—	Out-of-plane	Theoretical	[73]
WS_2	—	Out-of-plane	Theoretical	[70]	AlN	—	Out-of-plane	Theoretical	[73]
WSe_2	—	Out-of-plane	Theoretical	[70]	ZnO	—	Out-of-plane	Theoretical	[73]
WTe_2	> 350	Out-of-plane	Theoretical	[71]	Bi	463	In-plane	Theoretical	[81]
β-GeSe	212	In-plane	Theoretical	[77]	Sb	680	In-plane	Theoretical	[81]
GeS	RT	In-plane	Theoretical	[78]	As	478	In-plane	Theoretical	[81]
SnS	RT	In-plane	Theoretical	[78]	Te	> RT	In-plane	Theoretical	[82]
SnSe	RT	In-plane	Theoretical	[78]	d1T-$MoTe_2$	RT	Out-of-plane	Experimental	[12]
GeTe	570	In-plane	Theoretical	[79]	WTe_2	350	Out-of-plane	Experimental	[83]
SnTe	570	In-plane	Theoretical	[79]	α-In_2Se_3	RT	In-plane/out-of-plane	Experimental	[11]
SiTe	570	In-plane	Theoretical	[79]	β'-In_2Se_3	473	In-plane	Experimental	[84]
PbTe	—	In-plane	Theoretical	[80]	SnTe	270	In-plane	Experimental	[85]
SbN	1,700	In-plane	Theoretical	[72]	$CuInP_2S_6$	315	Out-of-plane	Experimental	[86]
BiP	~ 800	In-plane	Theoretical	[72]	BA_2PbCl_4	453	In-plane	Experimental	[87]
InSe	—	Out-of-plane	Theoretical	[73]					

mainly divided into six parts to illustrate the current situation of 2D vdW ferromagnetic and ferroelectric. In Section 2, we will introduce the 2D insulator ferromagnetic, such as CrI_3 and $Cr_2Ge_2Te_6$. In Section 3, we will review the 2D metallic ferromagnetic of Fe_3GeTe_2. In Sections 4 and 5, we will briefly discuss the 2D antiferromagnetic and 2D ferroelectric, respectively. Finally, we will provide a conclusion and give perspectives of future research areas in 2D vdW ferromagnetic and ferroelectric.

2 2D ferromagnetic insulator: CrI_3 and $Gr_2Ge_2Te_6$

2.1 CrI_3

Few- and monolayer (1L) CrI_3, with the strong intrinsic magnetocrystalline anisotropy and magnetism maintained in thin layers, have been extensively investigated both in theory and experiment since 2017. The structure schematic of CrI_3 is shown in Fig. 1(a), the Cr atoms are coordinated to six I atoms to form edge-sharing octahedral arranged in a hexagonal honeycomb lattice. And the magnetism arises from the super-exchange interaction between Cr atoms mediated by the spin-orbit coupling of I atoms. Previous research has shown that the bulk CrI_3 is a strongly anisotropic ferromagnet below the T_c of 61 K and the easy magnetization axis is perpendicular to the basal plane [88]. In 2017, a pioneering work of the ferromagnetism persisting down to monolayer in CrI_3 was done by group of Xu et al. Utilizing polar magneto-optical Kerr effect (MOKE) measurement, it was validated that monolayer CrI_3 is an intrinsic Ising ferromagnet with the T_c of 45 K. In Fig. 1(b), layer-dependence MOKE measurements of CrI_3 demonstrated that the ferromagnetic behavior was distinctly observed in the monolayer, while the net magnetization vanishes in bilayer CrI_3 because the adjacent two layers have opposite magnetic orientation and nearly compensate each other, giving rise to antiferromagnetic behavior, and the ferromagnetic behavior returns back in trilayer CrI_3. The extraordinary behavior indicates the strong layer-dependent coupling of magnetic order [13]. In addition, the helicity of ligand-field photoluminescence (PL) in CrI_3 was observed, which was determined by magnetic order, and hence the PL emission is regarded as a powerful tool to probe the magnetic phase of CrI_3. Figure 1(c) shows the circular polarization-resolved PL spectra of bilayer CrI_3 under different magnetic fields of −1, 0, 1 T, at 15 K, respectively. There remains no net circular polarization at 0 T and an anomalous anti-ferromagnetic interlayer interaction was observed in bilayer CrI_3 [89]. Subsequently, Klein et al. and Wu et al. further proved the anti-ferromagnetic coupling mechanism of bilayer CrI_3 through dual-gated and second-harmonic generation (SHG) methods, respectively. Klein et al. demonstrated the conductance measurement on the basis of graphite/bilayer CrI_3/graphite/h-BN device (Fig. 1(d)). Upon the anti-ferromagnetic configuration, the conductance is suppressed. However, a large and sudden increase in conductance takes place owing to the switch from anti-ferromagnetic to ferromagnetic state [90].

There still remain debates on the stacking order of CrI_3 at low temperature. Bulk and encapsulated few-layer CrI_3 have been reported to be monoclinic stacking at room temperature and switch to rhombohedral stacking at ~ 210 K [88, 91], in contrary, the BN-encapsulated bi- and few-layer CrI_3 and $CrCl_3$ are recently demonstrated to adopt monoclinic structure (point group C_{2h} (2/m)) at ~ 10 K [92–94]. Figure 1(e) shows the low-temperature SHG spectra of bilayer CrI_3. A giant nonreciprocal SHG signal arises from the broken time-reversal symmetry and spatial-inversion symmetry due to the layered anti-ferromagnetic order. The polarization-resolved SHG spectra show that the SHG signals of co-circularly polarized configuration are appreciable although the cross-circularly polarized SHG is predominant, indicating the monoclinic stacking order in bilayer CrI_3 [92]. However, most recent work systematically investigated the stacking order of 2–5L and bulk CrI_3 at 10 K by the linear and circular polarization-resolved Raman spectroscopy (Figs. 2(a) and 2(b)), validates rhombohedral stacking structure in both antiferromagnetic and ferromagnetic CrI_3 [95].

The ferromagnetic properties of 2D ferromagnetism CrI_3 are significantly sensitive to external perturbations, such as

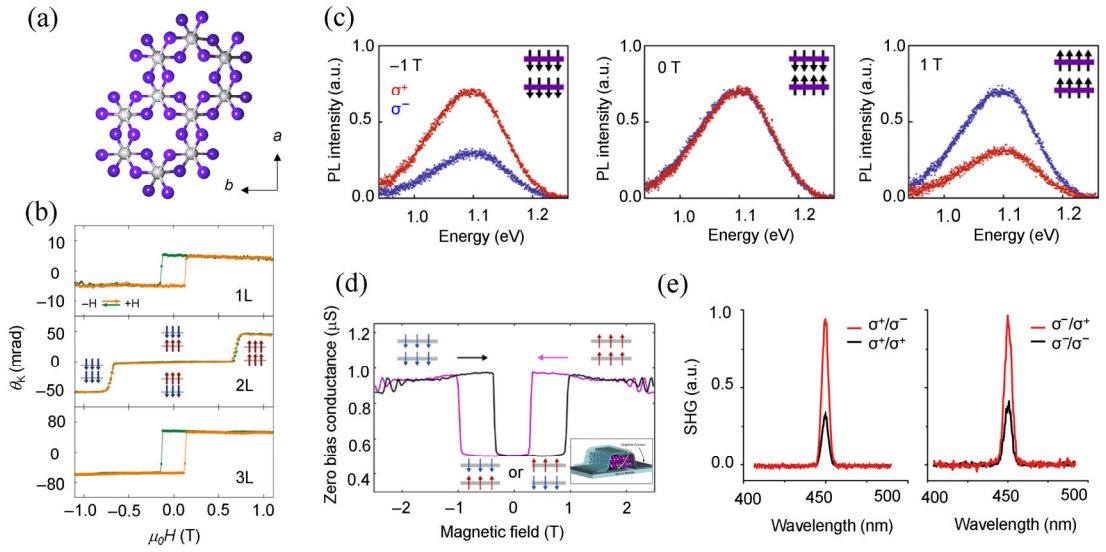

Figure 1 (a) Schematic crystal structure of CrI_3. (b) MOKE signal on monolayer, bilayer and trilayer CrI_3 flakes, respectively. (a) and (b) Reproduced with permission fromRef. [13], © Spring Nature 2017. (c) Circular polarization-resolved PL spectra of bilayer CrI_3 at 15 K under selected magnetic fields of −1 and 1 T, respectively (reproduced with permission from Ref. [89], © Spring Nature 2017). (d) Conductance through a bilayer CrI_3 tunnel barrier as a function of an out-of-plane applied magnetic field with 500 μV AC excitation (reproduced with permission from Ref. [90], © American Association for the Advancement of Science 2018). (e) Polarization resolved SHG spectra of bilayer CrI_3 (reproduced with permission from Ref. [92], © Spring Nature 2019).

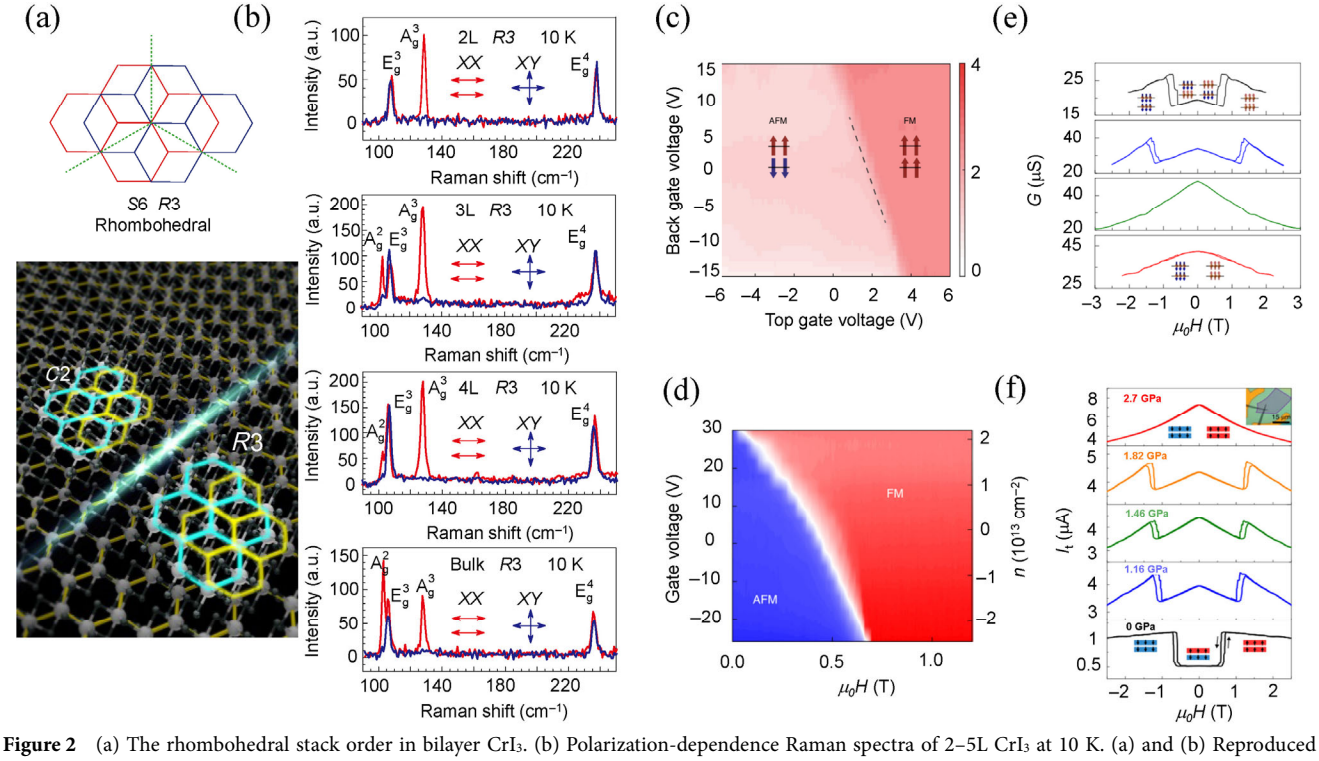

Figure 2 (a) The rhombohedral stack order in bilayer CrI_3. (b) Polarization-dependence Raman spectra of 2–5L CrI_3 at 10 K. (a) and (b) Reproduced with permission from Ref. [95], © Science China Press and Springer-Verlag GmbH Germany, part of Springer Nature 2019. (c) RMCD signal mapping changes with back gate and top gate voltage in bilayer CrI_3 (reproduced with permission from Ref. [96], © Springer Nature 2018). (d) The phase diagram of doping density-magnetic field at 4 K (reproduced with permission from Ref. [97], © Springer Nature 2018). (e) Tunnel conductance G as a function of magnetic field in a bilayer CrI_3 tunnel junction at 1.7 K under selected pressure of 0, 1, 1.8 and 0 GPa (reproduced with permission from Ref. [98], © Springer Nature 2019). (f) Tunneling current vs. magnetic field at a series of pressures (reproduced with permission from Ref. [99], © Springer Nature 2019).

electric field, electrostatic doping, strain or pressure. Xu et al. constructed a dual-gated bilayer CrI_3 device to explore gate-controlled magnetoelectric coupling effect (Fig. 2(c)). At a fixed magnetic field, the critical field for the meta-magnetic transition can be tuned by up to 30% by applying a gate voltage, which allows a gate-voltage driven phase transition from anti-ferromagnetic to ferromagnetic phase. Moreover, the two degenerate anti-ferromagnetic states could be distinguished by opposite slope after applying voltage [96]. Shan et al. demonstrated a control of the magnetic properties of both monolayer and bilayer CrI_3 by electrostatic doping in CrI_3-graphene vertical heterostructures [97] (Fig. 2(d)). For monolayer CrI_3, the saturation magnetization, coercive force and Curie temperature could be significantly enhanced by electron doping. For bilayer CrI_3, a transition from anti-ferromagnetic to ferromagnetic could be induced by electron doping with above ~ 2.5×10^{13} cm^{-2} doping concentration in the absence of a magnetic field. Furthermore, Xu et al. and Shan et al.

demonstrated the pressure-tuned/controlled CrI_3 magnetic states at the same time (Figs. 2(e) and 2(f)). The stacking order, structure phase and interlayer coupling could be tuned by external pressure, which provides a promising way to design magnetic phases and functionalities [98, 99].

2.2 $Cr_2Ge_2Te_6$

As another typical long-range ordered ferromagnet, $Cr_2Ge_2Te_6$ is a 2D Heisenberg soft ferromagnet with small magnetic anisotropy which means that the spin can be easily oriented towards all directions by external magnetic field. The crystal structures of $Cr_2Ge_2Te_6$ are shown in Fig. 3(a); the distorted honeycomb lattice of Cr atoms is sandwiched between two Ge and Te layers to form a single layer of $Cr_2Ge_2Te_6$. And the slight distortion of the Cr-Te_6 octahedral cage, together with spin-orbit coupling from the Cr atoms, leads to a small out-of-plane magnetocrystalline anisotropy. Scanning magneto-optical microscopy has been utilized to reveal the intrinsic long-range ferromagnetism [14]. The temperature-dependence Kerr rotations of 2–4L $Cr_2Ge_2Te_6$ show a T_c of 40 K with the help of a small out-of-plane magnetic field of 0.075 T to stabilize the magnetic moments and a strong dimensionality effect stemming from the low-energy excitations of magnons can be observed, indicating the interlayer magnetic coupling plays an important role in stabilizing the ferromagnetic order. This work serves as a benchmark to inspire more theoretical and experimental researches. In the same year, the identifications of ferromagnetic $Cr_2Ge_2Te_6$ thin flakes with various thickness have also been explored [100] (Fig. 3(b)). Electrostatic gating has long been regarded as an efficient method to manipulate the quantum state. In Fig. 3(c), Han et al. designed the ionic and Si-gated few-layer $Cr_2Ge_2Te_6$ FET, combined with micro-area Kerr measurements, a bipolar tunable magnetization behavior was observed by electron/hole doping in conduction/valence band. The mechanism of bipolar gate-tuned magnetism is ascribed to a rebalance of the spin-polarized band structure. The magnetism of $Cr_2Ge_2Te_6$ was also probed by electrical transport method [101]. As shown in Fig. 3(d), Shi et al. fabricated $Cr_2Ge_2Te_6$/Pt heterostructure and detected induced magneto-transport properties in Pt. The clear anomalous Hall effect (AHE) has been observed and the hysteresis loop persists to ~ 60 K, which is well consistent with the T_c obtained from the bulk magnetization measurements [102]. In addition, the observed slanted AHE loops with a narrow opening at 4 K, indicating the formation of magnetic domain, match with the results from low-temperature magnetic force microscopy (MFM). Inelastic light scattering provides approaches to measure various magnetic excitations, such as acoustic and optical magnons, and spinons. Raman spectroscopy has been conducted to explore the phonon dynamics and spin-phonon coupling in the system of $Cr_2Ge_2Te_6$ (Fig. 3(e)). A broad background signal above T_c can be seen owing to the thermal magnetic fluctuations, while near T_c, magnetic quasi-elastic scattering arising from the nearly 2D nature of its magnetism leads to a dramatic changes of E_{g1} and E_{g2} Raman modes [103]. In short, 2D Heisenberg ferromagnetic of $Cr_2Ge_2Te_6$ provides a platform for exploring underlying physics and highlights the feasibility for advancing emerging applications such as ultra-compact spintronics.

3 2D ferromagnetic metal: Fe_3GeTe_2

Unlike the 2D insulated ferromagnet mentioned above, Fe_3GeTe_2 is a metallic itinerant ferromagnet with higher T_c and better air stability in atmosphere [104]. Each layer consists of five sublayers with sandwich-like stacking order, in which iron atoms occupy three layers and the top and bottom sublayers are equivalent while the central one differs. The asymmetry of iron atoms leads to the occurrence of sizable magnetocrystalline anisotropy (Fig. 4(a)). Xu et al. systematically studied the temperature/thickness dependences employing the polar reflective magnetic circular dichroism (RMCD) method [105] (Fig. 4(b)). With increasing the temperature from 90 to 153 K, the hysteresis loop shrinks gradually and disappears at ~ 130 K, which indicates the T_c of monolayer is ~ 130 K. In Fig. 4(c), the thickness-temperature phase diagram can be divided into three sections: paramagnetic, single-domain ferromagnetic and labyrinthine-domain ferromagnet. This temperature dependent formation of magnetic domain implies a decrease in the ratio

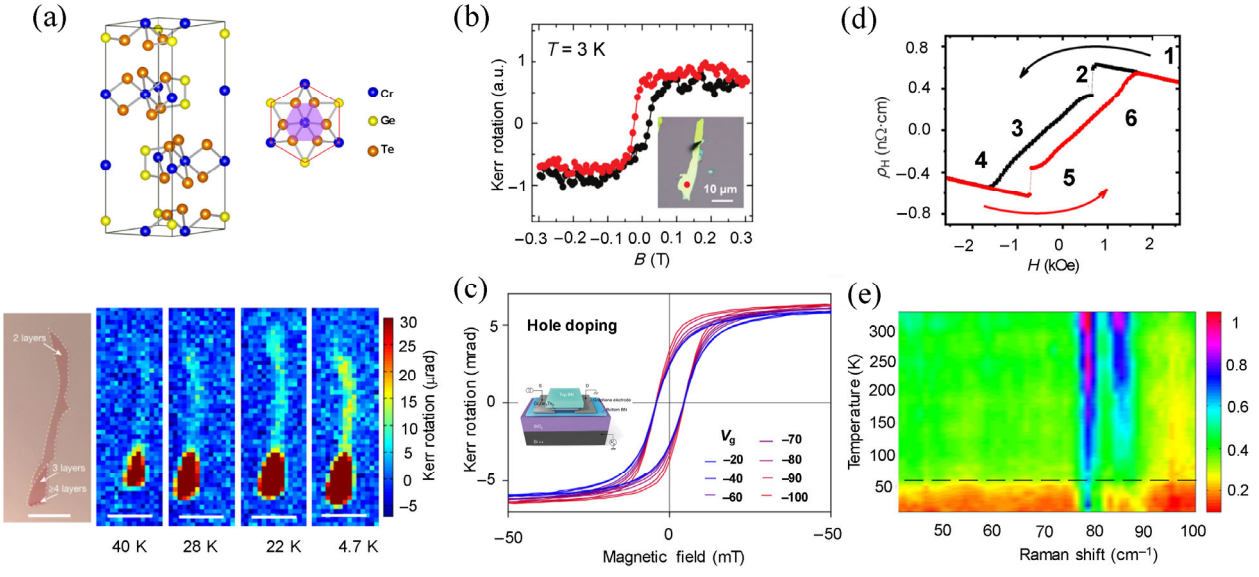

Figure 3 (a) Schematic crystal structure of $Cr_2Ge_2Te_6$ (top), the emergence of a Kerr rotation signal in the trilayer and bilayer $Cr_2Ge_2Te_6$ flake under 0.075 T, with the temperature decreasing from 40 to 4.7 K (bottom) (reproduced with permission from Ref. [14], © Springer Nature 2017). (b) The magnetic field dependence of the Kerr rotation on 2D $Cr_2Ge_2Te_6$ flake measured at 3 K (reproduced with permission from Ref. [100], © IOP Publishing Ltd 2017). (c) Kerr measurement of BN-encapsulated 3.5 nm $Cr_2Ge_2Te_6$ at 40 K for negative gate voltages (reproduced with permission from Ref. [101], © Springer Nature 2018). (d) Anomalous Hall hysteresis loop of $Cr_2Ge_2Te_6$ at 4 K (reproduced with permission from Ref. [102], © American Chemical Society 2019). (e) Temperature-dependence collinear Raman spectra of $Cr_2Ge_2Te_6$ for the E_{g1} and E_{g2} modes (reproduced with permission from Ref. [103], © IOP Publishing Ltd 2016).

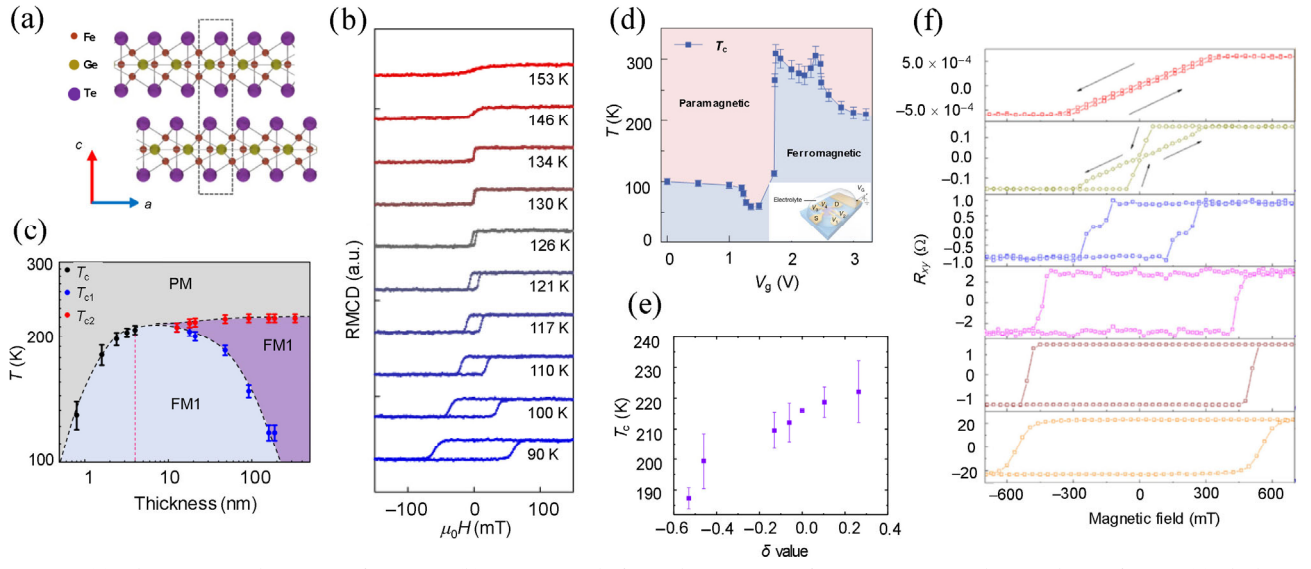

Figure 4 (a) Schematic crystal structure of Fe_3GeTe_2. (b) RMCD signal of monolayer Fe_3GeTe_2 from 90 to 153 K, indicating the T_c of 130 K. (c) Thickness–temperature phase diagram of Fe_3GeTe_2. (a)–(c) Reproduced with permission from Ref. [105], © Springer Nature 2018. (d) Gate-temperature phase diagram of trilayer Fe_3GeTe_2 (reproduced with permission from Ref. [31], © Springer Nature 2018). (e) Curie temperature varies with the ratio of iron element for 8 nm thick $Fe_{3+\delta}GeTe_2$ (reproduced with permission from Ref. [106], © Liu, S. S. et al. 2017). (f) Thickness-dependence Hall resistance of Fe_3GeTe_2 nanoflake at 2 K (reproduced with permission from Ref. [107], © Tan, C. et al. 2018).

of the strength of out-of-plane anisotropy to that of exchange interactions as the temperature increases. The electron concentration of 2D ferromagnetic Fe_3GeTe_2 is up to ~ 10^{21} cm^{-3}, making it easy to manipulate the magnetism through electrostatic control. The anomalous Hall resistance measurement of trilayer Fe_3GeTe_2 based on lithium-based electrolyte gated device [31] (Fig. 4(d)) demonstrated that T_c is only ~ 100 K and the hysteresis of R_{xy} curve also disappeared at zero gate voltage. However, when applying a positive gate voltage, T_c non-monotonically varies, reaching a value in excess of 300 K. The phenomenon is attributed to a substantial shift of the electronic bands and a large variation in the density of electron states near the Fermi level, which can be well interpreted by Stoner's criterion. Besides the gate-controlled method, the T_c also can be tuned via compositional modulation. Xiu et al. demonstrated a wafer-scale growth of Fe_3GeTe_2 with precisely controllable compositions and thickness by molecular beam epitaxy (MBE) method [106]. With increasing Fe composition, the T_c can be increased to ~ 220 K (Fig. 4(e)).The coercive field can be enhanced 50% by constructing Fe_3GeTe_2/MnTe heterostructure, arising from the exchange interaction at the ferromagnetic/anti-ferromagnetic interface. Furthermore, thickness-dependent AHE measurements validated that a hard magnetic phase with large coercive field occurred when the thickness of nanoflake is less than 200 nm [107] (Fig. 4(f)). In brief, owing to the larger magnetic anisotropy energy and higher T_c, metallic ferromagnet Fe_3GeTe_2 is regarded as promising candidates for the applications of magnetic RAM and magnetic tunnel junctions (MTJ).

4 2D anti-ferromagnetic materials: $FePS_3$ and $CrPS_4$

Despite the fact that anti-ferromagnets display zero net magnetization, anti-ferromagnets are insensitivity to external perturbations and have ultrafast spin dynamics in the terahertz range, making them become promising candidates in low-consumption, high-density and ultrafast information storage spintronic devices [108, 109]. Currently, various magnetic configurations have been discovered, such as the Heisenberg anti-ferromagnets of $MnPS_3$ and $MnPSe_3$ [110, 111], *XY*-type anti-ferromagnet of $NiPS_3$ [111] and Ising anti-ferromagnet of $FePS_3$ and $FePSe_3$ [110, 112]. In particular, the class of metal phosphorous trichalcogenide shows great importance in magnetism and spintronic applications. Here, we mainly introduce two kinds of anti-ferromagnetic $FePS_3$ and $CrPS_4$.

As shown in Fig. 5(a), in $FePS_3$ crystal, Fe atoms are coordinated with six S atoms, while P atoms are coordinated with three S atoms to form a tetrahedral $[PS_3]^{2-}$ unit, which further connected with another unit to form a $[P_2S_6]^{4-}$ unit. Connecting $[P_2S_6]^{4-}$ unit with six Fe atoms forms a honeycomb lattice. Raman spectroscopy could provide nondestructive techniques to probe complicated magnetic parameters. Figure 5(b) shows the Raman spectrum of monolayer $FePS_3$ grown by CVT. Below Néel temperature, a broad feature of low-frequency P_1 mode splits into four modes due to the presence of the zig-zag anti-ferromagnetic order which results in that the zone-boundary modes become active [29]. Temperature and thickness dependence of Raman features due to spin-phonon coupling have validated a magnetic persistence in $FePS_3$. The magnetic order can be maintained even down to monolayer limit [113] (Fig. 5(c)), and the Néel temperature of monolayer and bulk crystal is almost the same, indicating that intralayer spin coupling predominates the magnetic order. Furthermore, the pressured-induced phase transitions of $FePS_3$ were investigated (Fig. 5(d)). With a help of X-ray and electrical transport measurements, a transition process from insulator to metal at high pressure has been unambiguously observed, clarifying the relationship between lattice distortion and electron transition, perhaps which provides the insight into the origin of high-temperature superconductivity [114].

Spectroscopic studies are regarded as a powerful tool to explore the light-matter interaction for 2D magnets, nevertheless only a few of 2D magnets exhibit PL. Intriguingly, $CrPS_4$ is an anti-ferromagnetic semiconductor with near-infrared emitting. Lee et al. systematically investigated the optical and structure properties of single/few-layer $CrPS_4$ grown by CVT method, and temperature-dependent magnetization measurement demonstrates that the Néel temperature is ~ 37.9 K [115]. The relation of layer thickness and Raman features can be employed to

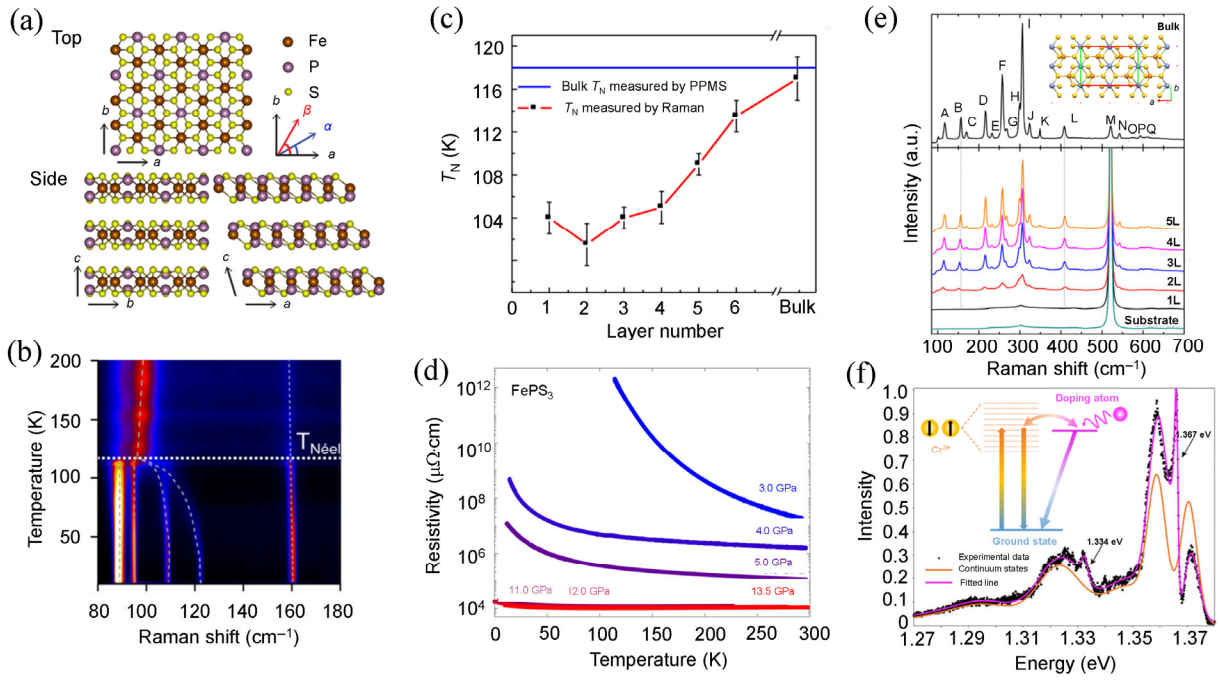

Figure 5 (a) Schematic crystal structure of $FePS_3$. (b) Temperature-dependence Raman spectrum of single-layer $FePS_3$. (a) and (b) Reproduced with permission from Ref. [29], © American Chemical Society 2016. (c) Thickness vs. Néel temperature of $FePS_3$ (reproduced with permission from Ref. [113], © IOP Publishing Ltd 2016). (d) Resistivity vs. temperature under the pressures from 3.0 to 13.5 GPa within a Bridgman anvil cell of $FePS_3$ (reproduced with permission from Ref. [114], © American Physical Society 2018). (e) Raman spectra of 1–5L and bulk $CrPS_4$, respectively (reproduced with permission from Ref. [115], © American Chemical Society 2017). (f) PL spectrum of $CrPS_4$ at 4 K (inset: the mechanism of Fano resonance in $CrPS_4$) (reproduced with permission from Ref. [116], © American Chemical Society 2020).

determine the thickness of a given $CrPS_4$ sample (Fig. 5(e)), which matches well with the data of atomic force microscope (AFM). Few-layer $CrPS_4$ shows strong PL emissions at ~ 1.32 and 1.33 eV originating from the continuum states of d band transitions localized at Cr^{3+} ions. Strikingly, a Fano resonance takes place due to the quantum interference of the continuum and discrete states when the time-reversal symmetry is broken by the anti-ferromagnetic orders (Fig. 5(f)). The discrete state stems from the extra atomic phosphorus [116]. Some novel concepts have been proposed to expand the scope of applications, such as the synaptic memory effects found in $CrPS_4$ [117]. The intrinsic characterization of 2D anti-ferromagnetic renders them excellent platforms for future applications.

5 2D ferroelectric materials: In_2Se_3 and $MoTe_2$

In the past decade, 2D layered vdW materials grow rapidly and exhibit various physical properties, which provide numerous opportunities to realize ferroelectricity in single-layer scale. Benefiting from the development of fabrication and probe technology, ferroelectric signal from several unit cells could be clearly observed and various 2D ferroelectric materials have been discovered. Here, 2D ferroelectric materials of In_2Se_3 and $MoTe_2$ will be discussed in detail.

As shown in Fig. 6(a), alternating Se and In atoms connect through covalent bond to form a single layer, and a quintuple layer of In_2Se_3 is constructed by stacking single layers together through weak vdW force. In general, it can be divided into five phases (α, β, γ, δ, κ) according to the stacking order. Actually, the α phase is predicted to be the most stable and can be maintained at room temperature. In 2017, room-temperature ferroelectricity with reversible spontaneous electric polarization in α-In_2Se_3 has been predicted via first-principles calculations and the out-of-plane (OOP) and in-plane (IP) polarization coexist [118]. In the same year, the experimental observation of OOP polarization in multilayer α-In_2Se_3 was reported [11]. The distinct ferroelectric domains could be distinguished by piezoresponse force microscopy (PFM) and the OOP polarization is potentially switchable in the samples with a thickness of ~ 10 nm (Fig. 6(b)). Afterwards, room-temperature robust intralayer ferroelectric in ultrathin flakes of α-In_2Se_3 has been realized (Fig. 6(c)). Intriguingly, the correlation between IP and OOP polarization is detected, in which the reversal of the OOP polarization by a vertical electric field also induces the rotation of the IP polarization. The behavior originates from the lateral movement of the central Se atomic layer induced by electric field [10]. Subsequently, a room-temperature ferroelectric diode was realized in graphene/α-In_2Se_3 heterojunctions (Fig. 6(d)). The switchable diode effect is due to OOP ferroelectric, and the interfacial Schottky barrier can be effectively tuned by switching the electric polarization with an applied voltage, leading to an on/off ratio up to ~ 10^5 [119]. Room-temperature IP ferroelectricity in β'-In_2Se_3 has also been observed (Fig. 6(e)). The IP polarization ferroelectricity is strongly tied to the formation of 1D superstructures aligned along one of the threefold rotational symmetric directions of the hexagonal lattice in the *c* plane [84].

As compared to III–V compounds of 2D ferroelectric, the realization of ferroelectricity in TMD is still lacking. On the basis of diverse components of TMD, there are various structural phases, such as 2H, 1T, 1T' and d1T. The 2H phase represents a stable semiconducting phase with trigonal prismatic coordination, while the 1T is an unstable metallic phase with octahedral coordination [120]. The 1T' phase refers to a distorted 1T phase with centrosymmetric structure in the form of zigzag M–M chains. The difference between 1T' and and d1T phases is mainly due to the different way of atomic distortion. Recently, the room-temperature ferroelectricity in monolayer d1T-$MoTe_2$ has been reported [12] (Fig. 6(f)). PFM measurement verified the existence of distinct ferroelectricity in d1T-$MoTe_2$ down to

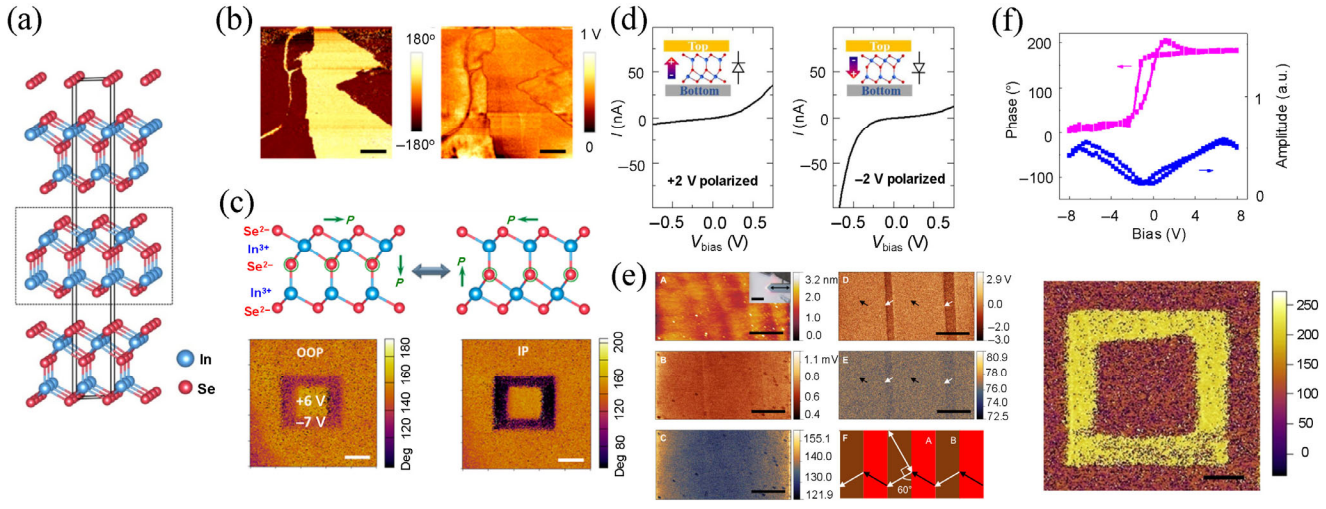

Figure 6 (a) Schematic crystal structure of In_2Se_3 (reproduced with permission from Ref. [118], © Ding, W. J. et al. 2017). (b) PFM phase and amplitude images of a thin α-In_2Se_3 flake, respectively (reproduced with permission from Ref. [11], © American Chemical Society 2017). (c) Schematic model of switching coupling for IP and OOP polarization (top). The phase images for both OOP and IP polarization of a 6 nm thick In_2Se_3 flake (bottom). Reproduced with permission from Ref. [10], © American Chemical Society 2018. (d) *I*–*V* curves of ferroelectric diodes with switchable rectifying behavior at 2 and −2 V, respectively (reproduced with permission from Ref. [119], © The Royal Society of Chemistry 2018). (e) PFM and AFM measurements for β'-In_2Se_3 (reproduced with permission from Ref. [84], © Zheng, C. X. 2018). (f) PFM phase hysteretic and phase image of monolayer d1T-$MoTe_2$, respectively (reproduced with permission from Ref. [12], © Yuan, S. G. et al. 2019).

monolayer limit; the OOP polarization can be switched by electric field. In contrast, no ferroelectricity was detected in the 2H-$MoTe_2$ phase. Theoretical calculations demonstrate that the spontaneous polarization of d1T-$MoTe_2$ is attributed to the form of trimerite structure induced by vertical displacements of the Te atoms. However, more efforts are needed to expand the family of 2D ferroelectric materials.

6 Perspective

In this review, we have taken a holistic view to introduce the present research situation and rapid progress of 2D ferromagnetic and ferroelectric materials, which provide a broad platform for theoretical and practical investigation. The instability and low T_c in such atomically thin ferromagnetic and ferroelectric layers limit their practical applications. At present, it is necessary to discover new 2D ferromagnetic and ferroelectric materials, it is necessary to develop new approaches to improve their stability and T_c, it is necessary to realize large-scale growth, which will make the journey to practical applications possible.

The interface physics of heterostructure geometry comprising 2D ferromagnetic and ferroelectric materials is a rich field that remains to be explored. Owing to the atomic-level flatness and various excellent properties of 2D materials, interfacial engineering of heterostructure will provide vital platforms for exploring new physical properties and constructing novel functional devices. Generally, three main mechanisms: interfacial charge transfer, interfacial built-in electric field and magnetoelectric coupling, make the proximity effect between layered vdW materials and 2D magnets/2D ferroelectric occur. To date, MTJ, multiferroics-based and spin-filtering devices etc., such as Fe_3GeTe_2/h-BN/Fe_3GeTe_2, graphene/CrI_3/graphene, graphene/$CrBr_3$/graphene, CrI_3/WSe_2, have been reported [121–124].

The emerging vdW magnets with well-defined layer thickness and atomic flatness are playing a vital role in the MTJ technology. Compared with the conventional non-vdW materials, 2D layered vdW MTJ with uniform thickness exhibits great advantages in all-area tunneling because the tunneling current is an exponential function of the barrier thickness. The 2D MTJ of Fe_3GeTe_2/h-BN/Fe_3GeTe_2 heterostructures have demonstrated a 160% magnetoresistance ratio [121]. The two metallic ferromagnetic layers are magnetically decoupled mediated via h-BN, which enable the realization of independent switching. Strikingly, a novel sandwiched heterostructures of graphene/CrI_3/graphene have also been realized with a record 19,000% magnetoresistance ratio [122]. The magnetic states of bilayer and few-layer CrI_3 switch with external magnetic field, which further influence the tunneling current. However, serious challenges concerning room temperature working, nonvolatility and low-power switching, are still remaining. High-density, low-power and nonvolatile memory is vital in solid-state electronic devices. Based on various types of storage media and different mechanisms, a variety of nonvolatile memories have been developed in recent years, such as Flash, M-RAM, Fe-RAM, PC-RAM and MF-RAM, etc. [125–129]. Utilizing the electric-control of dual-ion phase transformations method, multi-magnetic state transitions have been realized in $SrCoO_{2.5}$ at room temperature [130]. In multiferroic tunnel junctions of $La_{0.7}Sr_{0.3}MnO_3$/$BaTiO_3$/$La_{0.7}Sr_{0.3}MnO_3$, multi-nonvolatile resistive states have been realized, the switching speed and write current density are ~ 6 ns and ~ 3×10^3 A·cm^{-2}, respectively [129]. Furthermore, the realization of electric control of Néel spin-orbit torque can be observed in antiferromagnetic Mn_2Au/PMN-PT heterostructure with the driven-voltage of ~ 2 kV·cm^{-1}, realizing the reversal of in-plane uniaxial magnetic anisotropy by 90° [131]. However, the aforementioned devices are inevitably facing the problem of high-power consumption. Since the thickness of 2D materials is only a few atomic layers, the screening effect is drastically weakened, which makes it easier for modulating the electrical and magnetic properties through external electric field and magnetic field, and it is more conducive to reducing the power consumption of the device, even achieving near-zero power consumption. Hence, 2D ferromagnetic and ferroelectric materials provide a promising platform for developing nonvolatile memory devices. On the other hand, many of 2D ferroelectric materials have been predicted to be multiferroics with abundant physical properties, coupling with 2D ferromagnetism provides a significant and promising idea for nonvolatile spintronics and memories. The

2D ferroelectric material is utilized to provide a strong effective electric field at the interface. Theoretically, the strength of effective electric field is three orders of magnitude higher than the external applied electrostatic field. The long-range magnetic order can be tuned by combining the strong interfacial magnetoelectric coupling and weak screening effect, which highlight a bright future for the realization of energy-efficient nonvolatile memories.

The challenges still remain serious: 1) Lower T_c. At present, the typical T_c of 2D layered vdW ferromagnets is almost far away below room temperature. According to Mermin-Wagner theory [5], the critical temperature is mainly prohibited by exchange interaction and magnetic anisotropy. The T_c can be improved to ~ 300 K by means of ionic gating and chemical stoichiometric ratio tuning [31, 132]. More efforts are needed to overcome this constraint. 2) Unstable in air. Another important challenge is to discover 2D ferromagnetic and ferroelectric materials that are air-stable and insensitivity under ambient conditions, allowing them to work for a long time. In most cases, the current experimental operations are performed in the glove box, which limits the practical applications. Encapsulation by using few-layer h-BN as passivation is regarded as an effective way to prolong lifetime [133]. 3) Lacking of ferromagnetic or antiferromagnetic semiconductor. Future experiments are required to really realize the intrinsic magnetic semiconductor, although which have been predicted by first principle calculations. 4) The convinced mechanisms of spin-electron coupling and magnon in 2D system still lack, although which have been studied in 3D ferromagnetic insulator, such as YIG. Importantly, the spin-electron coupling and spin-wave can be harnessed to carve out a path to realize topological spin configurations like skyrmions, high-density, low-power data storage and computing devices [134]. Therefore, more experimental and theoretical works should be done to explore the fundamental physical and chemical properties in future.

Acknowledgements

We acknowledge financial support from the National Natural Science Foundation of China (Nos. 51602040 and 51872039), Science and Technology Program of Sichuan (No. M112018JY0025) and Scientific Research Foundation for New Teachers of UESTC (No. A03013023601007).

Reference

[1] Peierls, R. Quelques propriétés typiques des corps solides. *Ann. I. H. Poincaré*. **1935**, *5*, 177–222.
[2] Landau, L. D. Zur theorie der phasenumwandlungen II. *Phys. Z. Sowjet.* **1937**, *11*, 26–35.
[3] Geim, A. K.; Novoselov, K. S. The rise of graphene. *Nat. Mater.* **2007**, *6*, 183–191.
[4] Mermin, N. D.; Wagner, H. Absence of ferromagnetism or antiferromagnetism in one- or two-dimensional isotropic heisenberg models. *Phys. Rev. Lett.* **1966**, *17*, 1133–1136.
[5] Mermin, N. D. Crystalline order in two dimensions. *Phys. Rev.* **1968**, *176*, 250–254.
[6] Novoselov, K. S.; Geim, A. K.; Morozov, S. V.; Jiang, D.; Zhang, Y.; Dubonos, S. V.; Grigorieva, I. V.; Firsov, A. A. Electric field effect in atomically thin carbon films. *Science* **2004**, *306*, 666–669.
[7] Xi, X. X.; Zhao, L.; Wang, Z. F.; Berger, H.; Forró, L.; Shan, J.; Mak, K. F. Strongly enhanced charge-density-wave order in monolayer $NbSe_2$. *Nat. Nanotechnol.* **2015**, *10*, 765–769.
[8] Mak, K. F.; Lee, C.; Hone, J.; Shan, J.; Heinz, T. F. Atomically thin MoS_2: A new direct-gap semiconductor. *Phys. Rev. Lett.* **2010**, *105*, 136805.
[9] Fatemi, V.; Wu, S. F.; Cao, Y.; Bretheau, L.; Gibson, Q. D.; Watanabe, K.; Taniguchi, T.; Cava, R. J.; Jarillo-Herrero, P. Electrically tunable low-density superconductivity in a monolayer topological insulator. *Science* **2018**, *362*, 926–929.
[10] Cui, C. J.; Hu, W. J.; Yan, X. X.; Addiego, C.; Gao, W. P.; Wang, Y.; Wang, Z.; Li, L. Z.; Cheng, Y. C.; Li, P. et al. Intercorrelated in-plane and out-of-plane ferroelectricity in ultrathin two-dimensional layered semiconductor In_2Se_3. *Nano Lett.* **2018**, *18*, 1253–1258.
[11] Zhou, Y.; Wu, D.; Zhu, Y. H.; Cho, Y. J.; He, Q.; Yang, X.; Herrera, K.; Chu, Z. D.; Han, Y.; Downer, M. C. et al. Out-of-plane piezoelectricity and ferroelectricity in layered α-In_2Se_3 nanoflakes. *Nano Lett.* **2017**, *17*, 5508–5513.
[12] Yuan, S. G.; Luo, X.; Chan, H. L.; Xiao, C. C.; Dai, Y. W.; Xie, M. H.; Hao, J. H. Room-temperature ferroelectricity in $MoTe_2$ down to the atomic monolayer limit. *Nat. Commun.* **2019**, *10*, 1775.
[13] Huang, B.; Clark, G.; Navarro-Moratalla, E.; Klein, D. R.; Cheng, R.; Seyler, K. L.; Zhong, D.; Schmidgall, E.; McGuire, M. A.; Cobden, D. H. et al. Layer-dependent ferromagnetism in a van der Waals crystal down to the monolayer limit. *Nature* **2017**, *546*, 270–273.
[14] Gong, C.; Li, L.; Li, Z. L.; Ji, H. W.; Stern, A.; Xia, Y.; Cao, T.; Bao, W.; Wang, C. Z.; Wang, Y. et al. Discovery of intrinsic ferromagnetism in two-dimensional van der Waals crystals. *Nature* **2017**, *546*, 265–269.
[15] Dillon, J. F., Jr.; Kamimura, H.; Remeika, J. P. Magneto-optical properties of ferromagnetic chromium trihalides. *J. Phys. Chem. Solids* **1966**, *27*, 1531–1549.
[16] Suits, J. Faraday and kerr effects in magnetic compounds. *IEEE Trans. Magn.* **1972**, *8*, 95–105.
[17] Zhang, J.; Soon, J. M.; Loh, K. P.; Yin, J. H.; Ding, J.; Sullivian, M. B.; Wu, P. Magnetic molybdenum disulfide nanosheet films. *Nano Lett.* **2007**, *7*, 2370–2376.
[18] Botello-Méndez, A. R.; López-Urías, F.; Terrones, M.; Terrones, H. Metallic and ferromagnetic edges in molybdenum disulfide nanoribbons. *Nanotechnology* **2009**, *20*, 325703.
[19] Li, Y. F.; Zhou, Z.; Zhang, S. B.; Chen, Z. F. MoS_2 Nanoribbons: High stability and unusual electronic and magnetic properties. *J. Am. Chem. Soc.* **2008**, *130*, 16739–16744.
[20] Ataca, C.; Ciraci, S. Functionalization of single-layer MoS_2 honeycomb structures. *J. Phys. Chem. C* **2011**, *115*, 13303–13311.
[21] Ramasubramaniam, A.; Naveh, D. Mn-doped monolayer MoS_2: An atomically thin dilute magnetic semiconductor. *Phys. Rev. B* **2013**, *87*, 195201.
[22] Zhang, K. H.; Feng, S. M.; Wang, J. J.; Azcatl, A.; Lu, N.; Addou, R.; Wang, N.; Zhou, C. J.; Lerach, J.; Bojan, V. et al. Manganese doping of monolayer MoS_2: The substrate is critical. *Nano Lett.* **2015**, *15*, 6586–6591.
[23] Kochat, V.; Apte, A.; Hachtel, J. A.; Kumazoe, H.; Krishnamoorthy, A.; Susarla, S.; Idrobo, J. C.; Shimojo, F.; Vashishta, P.; Kalia, R. et al. Re doping in 2D transition metal dichalcogenides as a new route to tailor structural phases and induced magnetism. *Adv. Mater.* **2017**, *29*, 1703754.
[24] Zhao, P. J; Zheng, J. M.; Guo, P.; Jiang, Z. Y.; Cao, L. K.; Wan, Y. Electronic and magnetic properties of Re-doped single-layer MoS_2: A DFT study. *Comp. Mater. Sci.* **2017**, *128*, 287–293.
[25] Hu, A. M.; Wang, L. L.; Xiao, W. Z.; Xiao, G.; Rong, Q. Y. Electronic structures and magnetic properties in nonmetallic element substituted MoS_2 monolayer. *Comp. Mater. Sci.* **2015**, *107*, 72–78.
[26] Shi, H. L.; Pan, H.; Zhang, Y. W.; Yakobson, B. I. Strong ferromagnetism in hydrogenated monolayer MoS_2 tuned by strain. *Phys. Rev. B* **2013**, *88*, 205305.
[27] Kuo, C. T.; Neumann, M.; Balamurugan, K.; Park, H. J.; Kang, S.; Shiu, H. W.; Kang, J. H.; Hong, B. H.; Han, M.; Noh, T. W. et al. Exfoliation and Raman spectroscopic fingerprint of few-layer $NiPS_3$ van der Waals crystals. *Sci. Rep.* **2016**, *6*, 20904.
[28] Du, K. Z.; Wang, X. Z.; Liu, Y.; Hu, P.; Utama, M. I. B.; Gan, C. K.; Xiong, Q. H.; Kloc, C. Weak van der Waals stacking, wide-range band gap, and Raman study on ultrathin layers of metal phosphorus trichalcogenides. *ACS Nano* **2016**, *10*, 1738–1743.
[29] Lee, J. U.; Lee, S.; Ryoo, J. H.; Kang, S.; Kim, T. Y.; Kim, P.; Park, C. H.; Park, J. G.; Cheong, H. Ising-type magnetic ordering in atomically thin $FePS_3$. *Nano Lett.* **2016**, *16*, 7433–7438.

[30] Lin, M. W.; Zhuang, H. L.; Yan, J. Q.; Ward, T. Z.; Puretzky, A. A.; Rouleau, C. M.; Gai, Z.; Liang, L. B.; Meunier, V.; Sumpter, B. G. et al. Ultrathin nanosheets of $CrSiTe_3$: A semiconducting two-dimensional ferromagnetic material. *J. Mater. Chem. C* **2016**, *4*, 315–322.

[31] Deng, Y. J.; Yu, Y. J.; Song, Y. C.; Zhang, J. Z.; Wang, N. Z.; Sun, Z. Y.; Yi, Y. F.; Wu, Y. Z.; Wu, S. W.; Zhu, J. Y. et al. Gate-tunable room-temperature ferromagnetism in two-dimensional Fe_3GeTe_2. *Nature* **2018**, *563*, 94–99.

[32] Bonilla, M.; Kolekar, S.; Ma, Y. J.; Diaz, H. C.; Kalappattil, V.; Das, R.; Eggers, T.; Gutierrez, H. R.; Phan, M. H.; Batzill, M. Strong room-temperature ferromagnetism in VSe_2 monolayers on van der Waals substrates. *Nat. Nanotechnol.* **2018**, *13*, 289–293.

[33] O'Hara, D. J.; Zhu, T. C.; Trout, A. H.; Ahmed, A. S.; Luo, Y. K.; Lee, C. H.; Brenner, M. R.; Rajan, S.; Gupta, J. A.; McComb, D. W. et al. Room temperature intrinsic ferromagnetism in epitaxial manganese selenide films in the monolayer limit. *Nano Lett.* **2018**, *18*, 3125–3131.

[34] Zhuang, H. L.; Hennig, R. G. Stability and magnetism of strongly correlated single-layer VS_2. *Phys. Rev. B* **2016**, *93*, 054429.

[35] Kan, M.; Adhikari, S.; Sun, Q. Ferromagnetism in MnX_2 (X = S, Se) monolayers. *Phys. Chem. Chem. Phys.* **2014**, *16*, 4990–4994.

[36] Sivadas, N.; Daniels, M. W.; Swendsen, R. H.; Okamoto, S.; Xiao, D. Magnetic ground state of semiconducting transition-metal trichalcogenide monolayers. *Phys. Rev. B* **2015**, *91*, 235425.

[37] Zhuang, H. L.; Xie, Y.; Kent, P. R. C.; Ganesh, P. Computational discovery of ferromagnetic semiconducting single-layer $CrSnTe_3$. *Phys. Rev. B* **2015**, *92*, 035407.

[38] Zhang, W. B.; Qu, Q.; Zhu, P.; Lam, C. H. Robust intrinsic ferromagnetism and half semiconductivity in stable two-dimensional single-layer chromium trihalides. *J. Mater. Chem. C* **2015**, *3*, 12457–12468.

[39] He, J. J.; Ma, S. Y.; Lyu, P.; Nachtigall, P. Unusual Dirac half-metallicity with intrinsic ferromagnetism in vanadium trihalide monolayers. *J. Mater. Chem. C* **2016**, *4*, 2518–2526.

[40] Sun, Q. L.; Kioussis, N. Prediction of manganese trihalides as two-dimensional Dirac half-metals. *Phys. Rev. B* **2018**, *97*, 094408.

[41] Huang, C. X.; Zhou, J.; Wu, H. P.; Deng, K. M.; Jena, P.; Kan, E. J. Quantum anomalous Hall effect in ferromagnetic transition metal halides. *Phys. Rev. B* **2017**, *95*, 045113.

[42] Kumar, H.; Frey, N. C.; Dong, L.; Anasori, B.; Gogotsi, Y.; Shenoy, V. B. Tunable magnetism and transport properties in nitride MXenes. *ACS Nano* **2017**, *11*, 7648–7655.

[43] He, J. J.; Lyu, P.; Nachtigall, P. New two-dimensional Mn-based MXenes with room-temperature ferromagnetism and half-metallicity. *J. Mater. Chem. C* **2016**, *4*, 11143–11149.

[44] Zhang, Y. Z.; Wang, X.; Feng, Y.; Li, J.; Lim, C. T.; Ramakrishna, S. Coaxial electrospinning of (fluorescein isothiocyanate-conjugated bovine serum albumin)-encapsulated poly(ε-caprolactone) nanofibers for sustained release. *Biomacromolecules* **2006**, *7*, 1049–1057.

[45] Khazaei, M.; Arai, M.; Sasaki, T.; Chung, C. Y.; Venkataramanan, N. S.; Estili, M.; Sakka, Y.; Kawazoe, Y. Novel electronic and magnetic properties of two-dimensional transition metal carbides and nitrides. *Adv. Funct. Mater.* **2013**, *23*, 2185–2192.

[46] Yue, Y. L. Fe_2C monolayer: An intrinsic ferromagnetic MXene. *J. Magn. Magn. Mater.* **2017**, *434*, 164–168.

[47] Sun, Y. J.; Zhuo, Z. W.; Wu, X. J.; Yang, J. L. Room-temperature ferromagnetism in two-dimensional Fe_2Si nanosheet with enhanced spin-polarization ratio. *Nano Lett.* **2017**, *17*, 2771–2777.

[48] Zhao, T. S.; Zhou, J.; Wang, Q.; Kawazoe, Y.; Jena, P. Ferromagnetic and half-metallic FeC_2 monolayer containing C_2 dimers. *ACS Appl. Mater. Interfaces* **2016**, *8*, 26207–26212.

[49] Kan, M.; Zhou, J.; Sun, Q.; Kawazoe, Y.; Jena, P. The intrinsic ferromagnetism in a MnO_2 monolayer. *J. Phys. Chem. Lett.* **2013**, *4*, 3382–3386.

[50] Wu, J. C.; Peng, X.; Guo, Y. Q.; Zhou, H. D.; Zhao, J. Y.; Ruan, K. Q.; Chu, W. S.; Wu, C. Z. Ultrathin nanosheets of Mn_3O_4: A new two-dimensional ferromagnetic material with strong magnetocrystalline anisotropy. *Front. Phys.* **2018**, *13*, 138110.

[51] Zhang, K.; Khan, R.; Guo, H. Y.; Ali, I.; Li, X. L.; Lin, Y. X.; Chen, H. P.; Yan, W. S.; Wu, X. J.; Song, L. Room-temperature ferromagnetism in the two-dimensional layered Cu_2MoS_4 nanosheets. *Phys. Chem. Chem. Phys.* **2017**, *19*, 1735–1739.

[52] Sachs, B.; Wehling, T. O.; Novoselov, K. S.; Lichtenstein, A. I.; Katsnelson, M. I. Ferromagnetic two-dimensional crystals: Single layers of K_2CuF_4. *Phys. Rev. B* **2013**, *88*, 201402.

[53] Zhang, S. H.; Li, Y. W.; Zhao, T. S.; Wang, Q. Robust ferromagnetism in monolayer chromium nitride. *Sci. Rep.* **2014**, *4*, 5241.

[54] Zhang, Y.; Pang, J. M.; Zhang, M. G.; Gu, X.; Huang, L. Two-dimensional Co_2S_2 monolayer with robust ferromagnetism. *Sci. Rep.* **2017**, *7*, 15993.

[55] Naber, R. C. G.; Tanase, C.; Blom, P. W. M.; Gelinck, G. H.; Marsman, A. W.; Touwslager, F. J.; Setayesh, S.; de Leeuw, D. M. High-performance solution-processed polymer ferroelectric field-effect transistors. *Nat. Mater.* **2005**, *4*, 243–248.

[56] Jiang, A. Q.; Wang, C.; Jin, K. J.; Liu, X. B.; Scott, J. F.; Hwang, C. S.; Tang, T. A.; Lu, H. B.; Yang, G. Z. A resistive memory in semiconducting $BiFeO_3$ thin-film capacitors. *Adv. Mater.* **2011**, *23*, 1277–1281.

[57] Naber, R. C. G.; Asadi, K.; Blom, P. W. M.; De Leeuw, D. M.; De Boer, B. Organic nonvolatile memory devices based on ferroelectricity. *Adv. Mater.* **2010**, *22*, 933–945.

[58] Catalan, G.; Scott, J. F. Physics and applications of bismuth ferrite. *Adv. Mater.* **2009**, *21*, 2463–2485.

[59] Scott, J. F. Applications of modern ferroelectrics. *Science* **2007**, *315*, 954–959.

[60] Valasek, J. Piezo-electric and allied phenomena in rochelle salt. *Phys. Rev.* **1921**, *17*, 475–481.

[61] Fong, D. D.; Stephenson, G. B.; Streiffer, S. K.; Eastman, J. A.; Auciello, O.; Fuoss, P. H.; Thompson, C. Ferroelectricity in ultrathin perovskite films. *Science* **2004**, *304*, 1650–1653.

[62] Tsymbal, E. Y.; Kohlstedt, H. Tunneling across a ferroelectric. *Science* **2006**, *313*, 181–183.

[63] Zhong, W. L.; Wang, Y. G.; Zhang, P. L.; Qu, B. D. Phenomenological study of the size effect on phase transitions in ferroelectric particles. *Phys. Rev. B* **1994**, *50*, 698–703.

[64] Junquera, J.; Ghosez, P. Critical thickness for ferroelectricity in perovskite ultrathin films. *Nature* **2003**, *422*, 506–509.

[65] Gruverman, A.; Wu, D.; Lu, H.; Wang, Y.; Jang, H. W.; Folkman, C. M.; Zhuravlev, M. Y.; Felker, D.; Rzchowski, M.; Eom, C. B. et al. Tunneling electroresistance effect in ferroelectric tunnel junctions at the nanoscale. *Nano Lett.* **2009**, *9*, 3539–3543.

[66] Wang, H.; Liu, Z. R.; Yoong, H. Y.; Paudel, T. R.; Xiao, J. X.; Guo, R.; Lin, W. N.; Yang, P.; Wang, J.; Chow, G. M. et al. Direct observation of room-temperature out-of-plane ferroelectricity and tunneling electroresistance at the two-dimensional limit. *Nat. Commun.* **2018**, *9*, 3319.

[67] Böscke, T. S.; Müller, J.; Bräuhaus, D.; Schröder, U.; Böttger, U. Ferroelectricity in hafnium oxide thin films. *Appl. Phys. Lett.* **2011**, *99*, 102903.

[68] Müller, J.; Böscke, T. S.; Schröder, U.; Mueller, S.; Bräuhaus, D.; Böttger, U.; Frey, L.; Mikolajick, T. Ferroelectricity in simple binary ZrO_2 and HfO_2. *Nano Lett.* **2012**, *12*, 4318–4323.

[69] Shirodkar, S. N.; Waghmare, U. V. Emergence of ferroelectricity at a metal-semiconductor transition in a 1T monolayer of MoS_2. *Phys. Rev. Lett.* **2014**, *112*, 157601.

[70] Bruyer, E.; Di Sante, D.; Barone, P.; Stroppa, A.; Whangbo, M. H.; Picozzi, S. Possibility of combining ferroelectricity and Rashba-like spin splitting in monolayers of the 1T-type transition-metal dichalcogenides MX_2 (M = Mo, W; X = S, Se, Te). *Phys. Rev. B* **2016**, *94*, 195402.

[71] Yang, Q.; Wu, M. H.; Li, J. Origin of two-dimensional vertical ferroelectricity in WTe_2 bilayer and multilayer. *J. Phys. Chem. Lett.* **2018**, *9*, 7160–7164.

[72] Liu, C.; Wan, W. H.; Ma, J.; Guo, W.; Yao, Y. G. Robust ferroelectricity in two-dimensional SbN and BiP. *Nanoscale* **2018**, *10*, 7984–7990.

[73] Li, L.; Wu, M. H. Binary compound bilayer and multilayer with vertical polarizations: Two-dimensional ferroelectrics, multiferroics, and nanogenerators. *ACS Nano* **2017**, *11*, 6382–6388.

[74] Xu, B.; Xiang, H.; Xia, Y. D.; Jiang, K.; Wan, X. G.; He, J.; Yin, J.; Liu, Z. G. Monolayer $AgBiP_2Se_6$: An atomically thin ferroelectric semiconductor with out-plane polarization. *Nanoscale* **2017**, *9*, 8427–8434.

[75] Liu, F. C.; You, L.; Seyler, K. L.; Li, X. B.; Yu, P.; Lin, J. H.; Wang, X. W.; Zhou, J. D.; Wang, H.; He, H. Y. et al. Room-temperature

ferroelectricity in $CuInP_2S_6$ ultrathin flakes. *Nat. Commun.* **2016**, *7*, 12357.
[76] Song, W. S.; Fei, R. X.; Yang, L. Off-plane polarization ordering in metal chalcogen diphosphates from bulk to monolayer. *Phys. Rev. B* **2017**, *96*, 235420.
[77] Guan, S.; Liu, C.; Lu, Y.; Yao, Y.; Yang, S. A. Tunable ferroelectricity and anisotropic electric transport in monolayer β-GeSe. *Phys. Rev. B* **2018**, *97*, 144104.
[78] Wang, H.; Qian, X. F. Two-dimensional multiferroics in monolayer group IV monochalcogenides. *2D Mater*. **2017**, *4*, 015042.
[79] Wan, W. H.; Liu, C.; Xiao, W. D.; Yao, Y. G. Promising ferroelectricity in 2D group IV tellurides: A first-principles study. *Appl. Phys. Lett.* **2017**, *111*, 132904.
[80] Zhang, X. L.; Yang, Z. X.; Chen, Y. Novel two-dimensional ferroelectric PbTe under tension: A first-principles prediction. *J. Appl. Phys.* **2017**, *122*, 064101.
[81] Xiao, C. C.; Wang, F.; Yang, S. A.; Lu, Y. H.; Feng, Y. P.; Zhang, S. B. Elemental ferroelectricity and antiferroelectricity in group-V monolayer. *Adv. Funct. Mater.* **2018**, *28*, 1707383.
[82] Wang, Y.; Xiao, C. C.; Chen, M. G.; Hua, C. Q.; Zou, J. D.; Wu, C.; Jiang, J. Z.; Yang, S. A.; Lu, Y. H.; Ji, W. Two-dimensional ferroelectricity and switchable spin-textures in ultra-thin elemental Te multilayers. *Mater. Horiz.* **2018**, *5*, 521–528.
[83] Fei, Z. Y.; Zhao, W. J.; Palomaki, T. A.; Sun, B. S.; Miller, M. K.; Zhao, Z. Y.; Yan, J. Q.; Xu, X. D.; Cobden, D. H. Ferroelectric switching of a two-dimensional metal. *Nature* **2018**, *560*, 336–339.
[84] Zheng, C. X.; Yu, L.; Zhu, L.; Collins, J. L.; Kim, D.; Lou, Y. D.; Xu, C.; Li, M.; Wei, Z.; Zhang, Y. P. et al. Room temperature in-plane ferroelectricity in van der Waals In_2Se_3. *Sci. Adv.* **2018**, *4*, 7720.
[85] Chang, K.; Liu, J. W.; Lin, H. C.; Wang, N.; Zhao, K.; Zhang, A. M.; Jin, F.; Zhong, Y.; Hu, X. P.; Duan, W. H. et al. Discovery of robust in-plane ferroelectricity in atomic-thick SnTe. *Science* **2016**, *353*, 274–278.
[86] Belianinov, A.; He, Q.; Dziaugys, A.; Maksymovych, P.; Eliseev, E.; Borisevich, A.; Morozovska, A.; Banys, J.; Vysochanskii, Y.; Kalinin, S. V. $CuInP_2S_6$ room temperature layered ferroelectric. *Nano Lett.* **2015**, *15*, 3808–3814.
[87] You, L.; Liu, F. C.; Li, H. S.; Hu, Y. Z.; Zhou, S.; Chang, L.; Zhou, Y.; Fu, Q. D.; Yuan, G. L.; Dong, S. et al. In-plane ferroelectricity in thin flakes of van der Waals hybrid perovskite. *Adv. Mater.* **2018**, *30*, 1803249.
[88] McGuire, M. A.; Dixit, H.; Cooper, V. R.; Sales, B. C. Coupling of crystal structure and magnetism in the layered, ferromagnetic insulator CrI_3. *Chem. Mater.* **2015**, *27*, 612–620.
[89] Seyler, K. L.; Zhong, D.; Klein, D. R.; Gao, S. Y.; Zhang, X. O.; Huang, B.; Navarro-Moratalla, E.; Yang, L.; Cobden, D. H.; McGuire, M. A. et al. Ligand-field helical luminescence in a 2D ferromagnetic insulator. *Nat. Phys.* **2018**, *14*, 277–281.
[90] Klein, D. R.; MacNeill, D.; Lado, J. L.; Soriano, D.; Navarro-Moratalla, E.; Watanabe, K.; Taniguchi, T.; Manni, S.; Canfield, P.; Fernández-Rossier, J. et al. Probing magnetism in 2D van der Waals crystalline insulators via electron tunneling. *Science* **2018**, *360*, 1218–1222.
[91] Djurdjić Mijin, S.; Šolajić, A.; Pešić, J.; Šćepanović, M.; Liu, Y.; Baum, A.; Petrovic, C.; Lazarević, N.; Popović, Z. V. Lattice dynamics and phase transition in CrI_3 single crystals. *Phys. Rev. B* **2018**, *98*, 104307.
[92] Sun, Z. Y.; Yi, Y. F.; Song, T. C.; Clark, G.; Huang, B.; Shan, Y. W.; Wu, S.; Huang, D.; Gao, C. L.; Chen, Z. H. et al. Giant nonreciprocal second-harmonic generation from antiferromagnetic bilayer CrI_3. *Nature* **2019**, *572*, 497–501.
[93] Klein, D. R.; MacNeill, D.; Song, Q.; Larson, D. T.; Fang, S.; Xu, M. Y.; Ribeiro, R. A.; Canfield, P. C.; Kaxiras, E.; Comin, R. et al. Enhancement of interlayer exchange in an ultrathin two-dimensional magnet. *Nat. Phys.* **2019**, *15*, 1255–1260.
[94] Sivadas, N.; Okamoto, S.; Xu, X. D.; Fennie, C. J.; Xiao, D. Stacking-dependent magnetism in bilayer CrI_3. *Nano Lett.* **2018**, *18*, 7658–7664.
[95] Guo, K.; Deng, B. W.; Liu, Z.; Gao, C. F.; Shi, Z. T.; Bi, L.; Zhang, L.; Lu, H. P.; Zhou, P. H.; Zhang, L. B. et al. Layer dependence of stacking order in nonencapsulated few-layer CrI_3. *Sci. China Mater.* **2020**, *63*, 413–420.
[96] Huang, B.; Clark, G.; Klein, D. R.; MacNeill, D.; Navarro-Moratalla, E.; Seyler, K. L.; Wilson, N.; McGuire, M. A.; Cobden, D. H.; Xiao, D. et al. Electrical control of 2D magnetism in bilayer CrI_3. *Nat. Nanotechnol.* **2018**, *13*, 544–548.
[97] Jiang, S. W.; Li, L. Z.; Wang, Z. F.; Mak, K. F.; Shan, J. Controlling magnetism in 2D CrI_3 by electrostatic doping. *Nat. Nanotechnol.* **2018**, *13*, 549–553.
[98] Li, T. X.; Jiang, S. W.; Sivadas, N.; Wang, Z. F.; Xu, Y.; Weber, D.; Goldberger, J. E.; Watanabe, K.; Taniguchi, T.; Fennie, C. J. et al. Pressure-controlled interlayer magnetism in atomically thin CrI_3. *Nat. Mater.* **2019**, *18*, 1303–1308.
[99] Song, T. C.; Fei, Z. Y.; Yankowitz, M.; Lin, Z.; Jiang, Q. N.; Hwangbo, K.; Zhang, Q.; Sun, B. S.; Taniguchi, T.; Watanabe, K. et al. Switching 2D magnetic states via pressure tuning of layer stacking. *Nat. Mater.* **2019**, *18*, 1298–1302.
[100] Xing, W. Y.; Chen, Y. Y.; Odenthal, P. M.; Zhang, X.; Yuan, W.; Su, T.; Song, Q.; Wang, T. Y.; Zhong, J. N.; Jia, S. et al. Electric field effect in multilayer $Cr_2Ge_2Te_6$: A ferromagnetic 2D material. *2D Mater*. **2017**, *4*, 024009.
[101] Wang, Z.; Zhang, T. Y.; Ding, M.; Dong, B. J.; Li, Y. X.; Chen, M. L.; Li, X. X.; Huang, J. Q.; Wang, H. W.; Zhao, X. T. et al. Electric-field control of magnetism in a few-layered van der Waals ferromagnetic semiconductor. *Nat. Nanotechnol.* **2018**, *13*, 554–559.
[102] Lohmann, M.; Su, T.; Niu, B.; Hou, Y. S.; Alghamdi, M.; Aldosary, M.; Xing, W. Y.; Zhong, J. N.; Jia, S.; Han, W. et al. Probing magnetism in insulating $Cr_2Ge_2Te_6$ by induced anomalous hall effect in Pt. *Nano Lett.* **2019**, *19*, 2397–2403.
[103] Tian, Y.; Gary, M. J.; Ji, H. W.; Cava, R. J.; Burch, K. S. Magneto-elastic coupling in a potential ferromagnetic 2D atomic crystal. *2D Mater*. **2016**, *3*, 025035.
[104] Deiseroth, H. J.; Aleksandrov, K.; Reiner, C.; Kienle, L.; Kremer, R. K. Fe_3GeTe_2 and Ni_3GeTe_2—Two new layered transition-metal compounds: Crystal structures, HRTEM investigations, and magnetic and electrical properties. *Eur. J. Inorg. Chem.* **2006**, *2006*, 1561–1567.
[105] Fei, Z. Y.; Huang, B.; Malinowski, P.; Wang, W. B.; Song, T. C.; Sanchez, J.; Yao, W.; Xiao, D.; Zhu, X. Y.; May, A. F. et al. Two-dimensional itinerant ferromagnetism in atomically thin Fe_3GeTe_2. *Nat. Mater.* **2018**, *17*, 778–782.
[106] Liu, S. S.; Yuan, X.; Zou, Y. C.; Sheng, Y.; Huang, C.; Zhang, E. Z.; Ling, J. W.; Liu, Y. W.; Wang, W. Y.; Zhang, C. et al. Wafer-scale two-dimensional ferromagnetic Fe_3GeTe_2 thin films grown by molecular beam epitaxy. *npj 2D Mater. Appl.* **2017**, *1*, 30.
[107] Tan, C.; Lee, J.; Jung, S. G.; Park, T.; Albarakati, S.; Partridge, J.; Field, M. R.; McCulloch, D. G.; Wang, L.; Lee, C. Hard magnetic properties in nanoflake van der Waals Fe_3GeTe_2. *Nat. Commun.* **2018**, *9*, 1554.
[108] Jungwirth, T.; Marti, X.; Wadley, P.; Wunderlich, J. Antiferromagnetic spintronics. *Nat. Nanotechnol.* **2016**, *11*, 231–241.
[109] Baltz, V.; Manchon, A.; Tsoi, M.; Moriyama, T.; Ono, T.; Tserkovnyak, Y. Antiferromagnetic spintronics. *Rev. Mod. Phys.* **2018**, *90*, 015005.
[110] Wiedenmann, A.; Rossat-Mignod, J.; Louisy, A.; Brec, R.; Rouxel, J. Neutron diffraction study of the layered compounds $MnPSe_3$ and $FePSe_3$. *Solid State Commun.* **1981**, *40*, 1067–1072.
[111] Joy, P. A.; Vasudevan, S. Magnetism in the layered transition-metal thiophosphates MPS_3 (M = Mn, Fe, and Ni). *Phys. Rev. B* **1992**, *46*, 5425–5433.
[112] Taylor, B.; Steger, J.; Wold, A.; Kostiner, E. Preparation and properties of iron phosphorus triselenide, $FePSe_3$. *Inorg. Chem.* **1974**, *13*, 2719–2721.
[113] Wang, X. Z.; Du, K. Z.; Liu, F. Y. Y.; Hu, P.; Zhang, J.; Zhang, Q.; Owen, M. H. S.; Lu, X.; Gan, C. K.; Sengupta, P. et al. Raman spectroscopy of atomically thin two-dimensional magneticiron phosphorus trisulfide ($FePS_3$) crystals. *2D Mater*. **2016**, *3*, 031009.
[114] Haines, C. R. S.; Coak, M. J.; Wildes, A. R.; Lampronti, G. I.; Liu, C.; Nahai-Williamson, P.; Hamidov, H.; Daisenberger, D.; Saxena, S. S. Pressure-induced electronic and structural phase evolution in the van der Waals compound $FePS_3$. *Phys. Rev. Lett.* **2018**, *121*, 266801.
[115] Lee, J.; Ko, T. Y.; Kim, J. H.; Bark, H.; Kang, B.; Jung, S. G.; Park, T.; Lee, Z.; Ryu, S.; Lee, C. Structural and optical properties of single- and few-layer magnetic semiconductor $CrPS_4$. *ACS Nano* **2017**, *11*, 10935–10944.

[116] Gu, P. F.; Tan, Q. H.; Wan, Y.; Li, Z. L.; Peng, Y. X.; Lai, J. W.; Ma, J. C.; Yao, X. H.; Yang, S. Q.; Yuan, K. et al. Photoluminescent quantum interference in a van der Waals magnet preserved by symmetry breaking. *ACS Nano* **2020**, *14*, 1003–1010.

[117] Lee, M. J.; Lee, S.; Lee, S.; Balamurugan, K.; Yoon, C.; Jang, J. T.; Kim, S. H.; Kwon, D. H.; Kim, M.; Ahn, J. P. et al. Synaptic devices based on two-dimensional layered single-crystal chromium thiophosphate ($CrPS_4$). *NPG Asia Mater.* **2018**, *10*, 23–30.

[118] Ding, W. J.; Zhu, J. B.; Wang, Z.; Gao, Y. F.; Xiao, D.; Gu, Y.; Zhang, Z. Y.; Zhu, W. G. Prediction of intrinsic two-dimensional ferroelectrics in In_2Se_3 and other III_2-VI_3 van der Waals materials. *Nat. Commun.* **2017**, *8*, 14956.

[119] Wan, S. Y.; Li, Y.; Li, W.; Mao, X. Y.; Zhu, W. G.; Zeng, H. L. Room-temperature ferroelectricity and a switchable diode effect in two-dimensional α-In_2Se_3 thin layers. *Nanoscale* **2018**, *10*, 14885–14892.

[120] Kim, H. J.; Kang, S. H.; Hamada, I.; Son, Y. W. Origins of the structural phase transitions in $MoTe_2$ and WTe_2. *Phys. Rev. B* **2017**, *95*, 180101.

[121] Wang, Z.; Sapkota, D.; Taniguchi, T.; Watanabe, K.; Mandrus, D.; Morpurgo, A. F. Tunneling spin valves based on Fe_3GeTe_2/hBN/Fe_3GeTe_2 van der Waals heterostructures. *Nano Lett.* **2018**, *18*, 4303–4308.

[122] Wang, Z.; Gutiérrez-Lezama, I.; Ubrig, N.; Kroner, M.; Gibertini, M.; Taniguchi, T.; Watanabe, K.; Imamoğlu, A.; Giannini, E.; Morpurgo, A. F. Very large tunneling magnetoresistance in layered magnetic semiconductor CrI_3. *Nat. Commun.* **2018**, *9*, 2516.

[123] Ghazaryan, D.; Greenaway, M. T.; Wang, Z.; Guarochico-Moreira, V. H.; Vera-Marun, I. J.; Yin, J.; Liao, Y.; Morozov, S. V.; Kristanovski, O.; Lichtenstein, A. I. et al. Magnon-assisted tunnelling in van der Waals heterostructures based on $CrBr_3$. *Nat. Electron.* **2018**, *1*, 344–349.

[124] Zhong, D.; Seyler, K. L.; Linpeng, X.; Cheng, R.; Sivadas, N.; Huang, B.; Schmidgall, E.; Taniguchi, T.; Watanabe, K.; McGuire, M. A. et al. Van der Waals engineering of ferromagnetic semiconductor heterostructures for spin and valleytronics. *Sci. Adv.* **2017**, *3*, 1603113.

[125] Baibich, M. N.; Broto, J. M.; Fert, A.; Van Dau, F. N.; Petroff, F.; Etienne, P.; Creuzet, G.; Friederich, A.; Chazelas, J. Giant magnetoresistance of (001)Fe/(001)Cr magnetic superlattices. *Phys. Rev. Lett.* **1988**, *61*, 2472–2475.

[126] Binasch, G.; Grünberg, P.; Saurenbach, F.; Zinn, W. Enhanced magnetoresistance in layered magnetic structures with antiferromagnetic interlayer exchange. *Phys. Rev. B* **1989**, *39*, 4828–4830.

[127] Ko, C.; Lee, Y.; Chen, Y. B.; Suh, J.; Fu, D. Y.; Suslu, A.; Lee, S.; Clarkson, J. D.; Choe, H. S.; Tongay, S. et al. Ferroelectrically gated atomically thin transition-metal dichalcogenides as nonvolatile memory. *Adv. Mater.* **2016**, *28*, 2923–2930.

[128] Ding, K. Y.; Wang, J. J.; Zhou, Y. X.; Tian, H.; Lu, L.; Mazzarello, R.; Jia, C. L.; Zhang, W.; Rao, F.; Ma, E. Phase-change heterostructure enables ultralow noise and drift for memory operation. *Science* **2019**, *366*, 210–215.

[129] Huang, W. C.; Zhao, W. B.; Luo, Z.; Yin, Y. W.; Lin, Y.; Hou, C. M.; Tian, B. B.; Duan, C. G.; Li, X. G. A high-speed and low-power multistate memory based on multiferroic tunnel junctions. *Adv. Electron. Mater.* **2018**, *4*, 1700560.

[130] Lu, N. P.; Zhang, P. F.; Zhang, Q. H.; Qiao, R. M.; He, Q.; Li, H. B.; Wang, Y. J.; Guo, J. W.; Zhang, D.; Duan, Z. et al. Electric-field control of tri-state phase transformation with a selective dual-ion switch. *Nature* **2017**, *546*, 124–128.

[131] Chen, X. Z.; Zhou, X. F.; Cheng, R.; Song, C.; Zhang, J.; Wu, Y. C.; Ba, Y.; Li, H. B.; Sun, Y. M.; You, Y. F. et al. Electric field control of Néel spin–orbit torque in an antiferromagnet. *Nat. Mater.* **2019**, *18*, 931–935.

[132] May, A. F.; Ovchinnikov, D.; Zheng, Q.; Hermann, R.; Calder, S.; Huang, B.; Fei, Z. Y.; Liu, Y. H.; Xu, X. D.; McGuire, M. A. Ferromagnetism near room temperature in the cleavable van der Waals crystal Fe_5GeTe_2. *ACS Nano* **2019**, *13*, 4436–4442.

[133] Shcherbakov, D.; Stepanov, P.; Weber, D.; Wang, Y. X.; Hu, J.; Zhu, Y. L.; Watanabe, K.; Taniguchi, T.; Mao, Z. Q.; Windl, W. et al. Raman spectroscopy, photocatalytic degradation, and stabilization of atomically thin chromium tri-iodide. *Nano Lett.* **2018**, *18*, 4214–4219.

[134] Fert, A.; Cros, V.; Sampaio, J. Skyrmions on the track. *Nat. Nanotechnol.* **2013**, *8*, 152–156.